Editors' Suggestion

On-Chip Quantum-Dot Light Source for Quantum-Device Readout

Y.-Y. Liu, J. Stehlik, X. Mi, T. R. Hartke, M. J. Gullans, and J. R. Petta
Department of Physics, Princeton University, Princeton, New Jersey 08544, USA

(Received 27 July 2017; revised manuscript received 5 December 2017; published 29 January 2018)

We use microwave radiation generated by a semiconductor double-quantum-dot (DQD) micromaser for charge-state detection. A cavity is populated with $n_c \sim 6000$ photons by driving a current through an emitter DQD. These photons are used to sense the charge state of a target DQD that is located at the opposite end of the cavity. The charge dynamics in the target DQD influences the output power and emission frequency of the maser. Three different readout mechanisms are compared. The detection scheme requires no cavity input field and may potentially be used to improve the scalability of semiconductor and superconducting qubit readout technologies.

DOI: 10.1103/PhysRevApplied.9.014030

I. INTRODUCTION

Quantum-state readout is a crucial component of any quantum computing architecture. For semiconductor quantum dots, charge-state readout has been performed using quantum point contacts [1] and quantum dots [2] as detectors. Electronic spin states can also be resolved using spin-to-charge conversion, which relies on spin-selective tunneling and sensitive charge-state detection [3,4]. To increase measurement bandwidths, conventional dc transport measurement approaches have, to a large extent, been replaced by rf and microwave frequency reflectometry setups [5–7]. In particular, the circuit quantum electrodynamics (cQED) architecture allows for dispersive readout of superconducting qubits [8–11], as well as semiconductor charge and spin qubits [12–19].

Both rf-reflectometry and cQED measurement implementations rely on costly room-temperature microwave sources, rf components, and coaxial lines that occupy a significant amount of space in a dilution refrigerator. As one scales to many qubits, the resource requirements increase dramatically. Moreover, to suppress the room-temperature microwave background, a typical attenuation of 60–70 dB is required in the coax lines connecting the signal generator to the quantum device (approximately 10 mK). To reduce the experimental complexity, the source would ideally be isolated from the 300-K environment.

Over the past ten years, it has been shown that a variety of voltage-biased quantum devices generate microwave frequency photons. For example, voltage-biased Cooper-pair boxes and superconducting quantum intereference devices embedded in superconducting cavities have been shown to mase [20,21]. Cavity-coupled semiconductor double quantum dots (DQDs) can serve as an electrically tunable maser gain medium [22–24]. These devices are fabrication compatible with other qubits and they can be integrated on the same chip. It is therefore of interest to determine if these devices, which already operate at millikelvin temperatures, can be utilized as microwave frequency sources in quantum computing experiments [25].

In this Letter, we show that microwave frequency photons generated by a cavity-coupled DQD can be used to sensitively read out the charge stability diagram of a second DQD that is located in the same cavity. A source-drain bias is applied across an emitter DQD (EDQD) and results in above-threshold masing. The photons generated by the EDQD are used to sense a target DQD (TDQD) that is located in the same cavity. Charge dynamics in the TDQD influence the maser emission, changing its output power and emission frequency, allowing for charge-state readout in future quantum-information-processing applications.

We explore three different readout approaches. In the first approach, the total power emitted by the cavity is measured and used to reconstruct the TDQD charge stability diagram. In the second approach, the EDQD emission frequency, which is dependent on the charge state of the TDQD, is used to measure the TDQD charge stability diagram by mapping out the maser emission frequency as a function of the TDQD gate voltages. In the third approach, we measure the power emitted into a narrow band centered around the free-running maser frequency. Shifts in the emission frequency significantly change the narrow-band power, allowing us to detect TDQD interdot charge transitions. We compare the back-action of the TDQD on the maser to expectations from semiclassical theory and find qualitative agreement.

While, in our experiment, we measure the charge stability diagram of the TDQD, our approach is directly applicable to quantum-state readout in singlet-triplet qubits [12]. Furthermore, the target system in these experiments could, in principle, be replaced with any other cavity-coupled qubit, such as a superconducting transmon. No external cavity drive is required in our experiments,

further supporting the use of a DQD maser as a light source for quantum-state readout in quantum computation architectures.

II. DEVICE DESCRIPTION

Figure 1(a) captures the important elements of our experimental setup. The EDQD and the TDQD are coupled to a microwave cavity. To serve as a microwave source, the EDQD is source-drain biased, which results in single-electron tunneling events and microwave frequency photon emission into the cavity mode [24]. These cavity photons are used to sense the charge state of the TDQD.

An optical micrograph of the device is shown in Fig. 1(b). The cavity consists of a $\lambda/2$ superconducting resonator with resonance frequency $f_c = 7596$ MHz and linewidth $\kappa_{\rm tot}/2\pi = 1.77$ MHz. The cavity is designed to have output (input) coupling rates $\kappa_{\rm out}/2\pi = 0.8$ MHz ($\kappa_{\rm in}/2\pi =$ 0.04 MHz). The InAs nanowire DQDs are located at opposite ends of the cavity near the voltage antinodes. The confinement potential of the TDQD is created by voltage biasing the five bottom gates labeled B_L^T, L^T, C^T, R^T, and B_R^T in Fig. 1(c). Independent control of the EDQD is achieved using a separate set of bottom gates. We further define source and drain Ohmic contacts using electron-beam lithography. In contrast with our previous work, the source contacts to the EDQD and TDQD are electrically decoupled such that the source-drain bias voltages can be independently controlled [26]. The drain electrode of each DQD is connected to the microwave resonator. Coupling between a charge trapped in the DQD confinement potential and the electric field of the cavity leads to an electric dipole interaction with strength $g_c/2\pi \approx 30$–40 MHz [23].

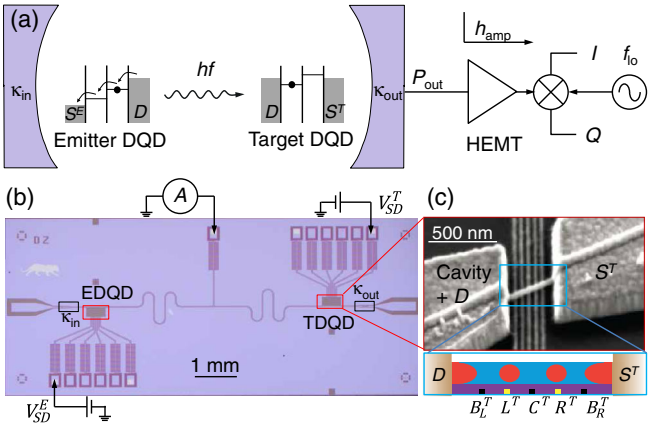

FIG. 1. (a) The experiment consists of a cavity containing two DQDs. A dc-biased EDQD mases and populates the cavity with microwave frequency photons. These photons are used to read out the charge state of the TDQD. (b) Optical microscope image showing the cavity and the positions of the EDQD and the TDQD. (c) (Upper panel) Scanning electron micrograph of a nanowire DQD. (Lower panel) The DQD confinement potential is defined using five bottom gates.

III. CHARACTERIZATION OF THE EMITTER DOUBLE QUANTUM DOT

We first characterize the microwave field emitted by the EDQD. For these measurements, the TDQD source-drain bias $V_{\rm SD}^T = 0$ and the gates are tuned such that the TDQD is in Coulomb blockade, where the charge number is fixed. In this configuration, the TDQD will not have any impact on the cavity field. The EDQD is configured to emit photons by applying a finite source-drain bias $V_{\rm SD}^E = 2$ mV, which results in single-electron-tunneling events and a current as high as $I_e = 9$ nA. The interdot charge transition leads to photon emission and, in a high-quality-factor cavity, a transition to a masing state [24].

To measure the emitted radiation, the cavity output field is amplified using a high-electron-mobility transistor (HEMT) amplifier and detected with a spectrum analyzer. Figure 2(a) shows the power spectral density $S(f)$ of the radiation emitted from the cavity, along with a fit to a Lorentzian. The best-fit parameters yield the emission frequency $f_e =$ 7595.68 MHz and FWHM = 8 kHz. We obtain a total output power $P_{\rm out} = 0.16$ pW by integrating over $S(f)$. The emission power yields an intracavity photon number $n_c = P_{\rm out}/(hf_e\kappa_{\rm out}) \approx 6000$ given $\kappa_{\rm out}/2\pi = 0.8$ MHz. The FWHM is 200 times narrower than the bare cavity linewidth, which is suggestive of masing.

The output field can be examined in more detail by measuring IQ (in-phase and quadrature-phase) histograms. To acquire the histograms, the cavity output field is first amplified with a HEMT and then demodulated into the in-phase (I) and quadrature-phase (Q) components by a local reference set to a frequency $f_{\rm lo} = f_c$ [26]. Figure 2(b) shows an IQ histogram obtained by accumulating 1.7×10^7 IQ samples at a rate of 12.3 MHz. The histogram has a ring shape that is consistent with coherent emission [24]. The threshold behavior of this device was also examined in a previous publication, with a threshold current $I_{\rm th} = 6.1$ nA and an operating current $I_e = 9$ nA [24]. Combined, these data sets show that the voltage-biased EDQD can serve as a coherent source that populates the cavity with approximately 6000 photons. These photons may

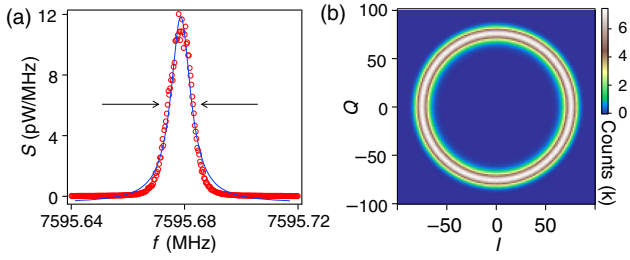

FIG. 2. (a) Power spectral density of the radiation emitted by the EDQD (the circles) and a fit to a Lorentzian (the solid line) with FWHM = 8 kHz. (b) The IQ histogram of the output field is consistent with a coherent source.

be used to read out the charge state of the TDQD, as is demonstrated in the following sections of this paper.

IV. TARGET-DOUBLE-QUANTUM-DOT CHARGE-STATE DETECTION

In this section, we provide a brief overview of charge-state readout in quantum dots and then compare several different approaches for measuring the charge stability diagram of the TDQD. We first measure the stability diagram using standard cavity input-output readout, where an input tone is provided by an external microwave generator that populates the cavity with photons. These data are then compared with charge stability diagrams that are obtained by measuring the total power emitted from the cavity when it is populated with EDQD photons. Two additional transduction methods are examined that are based on the effect that charge dynamics in the TDQD have on the emission properties of the EDQD. Specifically, we show that the TDQD charge stability diagram can be reconstructed by measuring the emission frequency of the EDQD and the narrow-band power emitted by the EDQD. Finally, we examine theoretical expectations of the back-action of the TDQD on the maser and find quantitative agreement with the data.

A. Charge-state readout through measurements of the cavity transmission

In quantum-dots, state readout is performed using the charge degree of freedom. For example, the conductance of a quantum point contact will sensitively depend on the charge configuration of the neighboring dots which are being probed [2,27]. In the cQED architecture, readout is performed by sensing the dispersive phase shift of a coupled cavity. For quantum dots, this dispersive shift is a sensitive differential charge meter that tests whether two electronic energy levels are nearly resonant with the cavity, but it cannot be used to directly measure absolute charge occupancies. Differential charge sensing is not a severe limitation, as it can be used for singlet-triplet spin state readout based on the Pauli exclusion principle [12,28].

The conventional cavity input-output readout approach on the TDQD is illustrated in Fig. 3(a). Here, the cavity is driven by an input tone of frequency $f_{\rm in}$ and power $P_{\rm in} \approx -112$ dBm that results in approximately $n_c \approx 10$ intracavity photons. The resulting cavity output is amplified with a HEMT and demodulated by a local reference having a frequency $f_{\rm lo} = f_{\rm in}$. Both the phase shift $\Delta\phi$ and the power gain $G = CP_{\rm out}/P_{\rm in}$ can be extracted from the cavity transmission. Here, the constant C is set such that $G = 1$, with $f_{\rm in} = f_c$ and both DQDs in Coulomb blockade [23,26]. Figure 3(c) plots G as a function of the TDQD gate voltages with $f_{\rm in} = f_c$ and $V^T_{\rm SD} = 0$. For this data set, the EDQD is in idle mode, with $V^E_{\rm SD} = 0$ and the gate voltages tuned to Coulomb blockade. These measurements

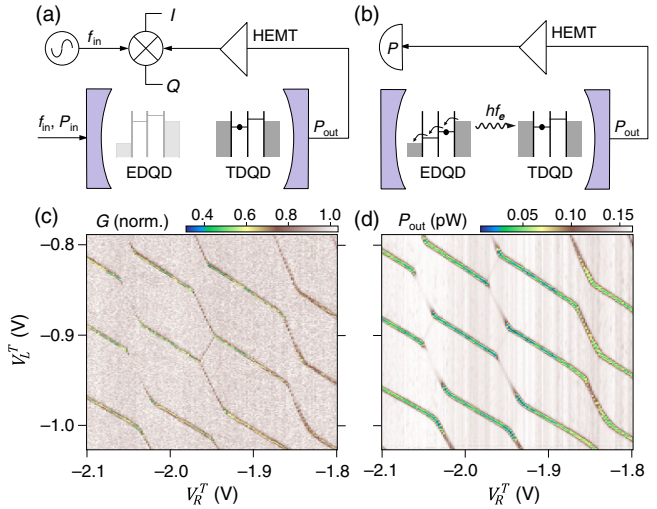

FIG. 3. (a) Circuit used to measure the TDQD charge stability diagram by driving the cavity with a weak input tone while the EDQD is in Coulomb blockade. (b) Photons emitted from the EDQD can be used to measure the charge stability diagram of the TDQD in the absence of a cavity input tone. (c) Gain, G, measured with the method shown in (a) as a function of V_L^T and V_R^T, revealing the TDQD charge stability diagram. (d) $P_{\rm out}$ measured with the method shown in (b) as a function of V_L^T and V_R^T also reveals the TDQD charge stability diagram.

reveal the TDQD charge stability diagram, consistent with previous measurements of cavity-coupled InAs nanowire DQDs [23].

B. Charge-state readout through measurements of the total cavity output power

To make a comparison with cavity input-output readout, we now turn off the cavity input tone and configure the EDQD in the "on state," such that it is emitting coherent radiation as shown in Fig. 2. We then measure the output power $P_{\rm out}$ and plot it as a function of V_L^T and V_R^T in Fig. 3(d). Writing the cavity output field complex amplitude as $\alpha = I + iQ$, $P_{\rm out}$ is determined from measurements of $\langle \alpha^* \alpha \rangle = \langle I^2 + Q^2 \rangle$. The IQ data are processed using a digital filter of 2.6 MHz bandwidth that covers the entire cavity linewidth, and $\langle I^2 + Q^2 \rangle$ therefore captures the total emitted power [29]. The scenario is equivalent to a power meter measuring over a wide bandwidth as illustrated in Fig. 3(b). The data in Fig. 3(d) show that measurements of $P_{\rm out}$ can be used to extract the TDQD charge stability diagram.

C. Impact of charge dynamics in the TDQD on the emission properties of the EDQD

We now more carefully examine the readout mechanism by studying the effect that the TDQD charge configuration has on the emission properties of the EDQD. Figure 4(a) shows a high-resolution measurement of $P_{\rm out}$ near one of

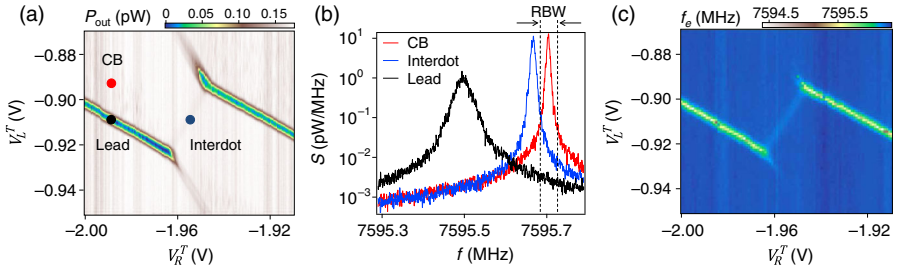

FIG. 4. (a) Total output power P_{out} as a function of V_L^T and V_R^T near a TDQD interdot charge transition. Here, the EDQD emission is used to populate the cavity with measurement photons. (b) $S(f)$ measured with the TDQD in Coulomb blockade (CB), at an interdot transition, and at a left-dot charge transition (lead). The dashed lines indicate the frequency window that the emission is integrated over in the narrow-band measurement approach. (c) f_e as a function of V_L^T and V_R^T. In these data, both single-dot and interdot charge transitions are visible.

the TDQD interdot charge transitions in Fig. 3(d). These data are acquired in the absence of a cavity input tone and with the EDQD emitting photons. The left-dot and right-dot charge transitions are visible in these data, while the visibility of the interdot charge transition is significantly less than in the data shown in Fig. 3(c).

To better understand what sets the visibility of the charge transitions in these data, we measure $S(f)$ of the emitted radiation with the gate voltages of the TDQD tuned to different regions of the TDQD charge stability diagram. Figure 4(b) shows measurements of $S(f)$ with the TDQD configured in Coulomb blockade, at the interdot charge transition, and at a left-dot charge transition. With the TDQD configured in Coulomb blockade, the emission peak in $S(f)$ is centered at $f_e^0 = 7595.68$ MHz. When the TDQD is configured to a left-dot charge transition, the emission peak shifts down in frequency by 214 kHz, the maximum $S(f)$ is reduced by approximately a factor of 10, and the peak in $S(f)$ is significantly broader, yielding a total power reduction by a factor of 3. By comparison, with the TDQD configured at the interdot charge transition, the emission peak is shifted down in frequency by only 37 kHz. The emission peak has a height and width that is comparable to the data acquired with the TDQD in Coulomb blockade. Therefore, it is difficult to resolve the interdot charge transitions in measurements of the total emitted power P_{out}. However, since the emission peak shifts by an amount that is much greater than the FWHM of the emission peak (approximately 8 kHz), measurements of the emission frequency may be used to reconstruct the TDQD charge stability diagram.

By fitting $S(f)$ to a Lorentzian at every point in the TDQD charge stability diagram, we can extract f_e as a function of V_L^T and V_R^T. A plot of the extracted f_e is shown in Fig. 4(c) and is much more sensitive to the interdot charge transition. Therefore a measurement of f_e can, in principle, be used to read out the device. The approach is similar to the cQED readout of transmon qubits, where the state-dependent dispersive shift of the cavity is used for readout [8,9]. In the most natural extension of this work, our readout scheme would be used to distinguish singlet and triplet states in a doubly occupied DQD. Here, due to the singlet-triplet splitting, only the singlet state will produce a cavity shift at the interdot charge transition [12].

To understand the backaction of the TDQD on the maser emission, we note that the maser and the TDQD reside in the same cavity. As such, any dispersive shift induced by the TDQD will manifest as a shift in the maser emission frequency. The backaction on the emission amplitude will be strong if the TDQD is at a dissipative charge transition (a lead transition) but will be weak at a coherent interdot transition where photon loss is negligible. In addition, the maser readout of charge transitions has a broader linewidth than does conventional readout. This broadening is due to the electric field coming from the large intracavity photon number and is analogous to the ac Stark shift.

It is important to note here that, in general, we do not know the phase of the maser emission, and that previous work showed that the coherence time of the maser is only on the order of 10 μs [26]. Even with improved maser coherence, the standard phase-measurement technique employed in cQED needs to be modified. This is the case due to the fact that, in our readout scheme, it is the maser emission frequency itself that depends on the charge state of the TDQD. Thus, our readout consists of discrimination between two different emission frequencies, rather than the phase response of an externally applied cavity probe tone.

D. Semiclassical analysis of the backaction of the TDQD on the maser

In order to understand the process of the TDQD backaction on the maser output, further experimental and theoretical investigation is needed. Here, we provide a semiclassical theoretical analysis of the backaction using rate equations when the target device is placed in the same cavity as the emitter. The hybrid EDQD-TDQD-cavity system can be described as the EDQD coupled to an effective cavity with variable effective frequency $\tilde{f}_c$ and linewidth $\tilde{\kappa}_{\text{tot}}$, which depend on the state of the TDQD. We can then use our previously developed theory of threshold

behavior in a semiconductor single-atom maser to predict the maser emission power as a function of the state of the TDQD [24].

When the intracavity photon number is small enough to neglect the saturation of two-level systems, both DQDs contribute to the susceptibility χ, which we separate into a real χ' and imaginary χ'' part describing the gain and cavity pull, respectively. We further separate the gain coefficient $\chi' = \chi'_t + \chi'_e$ and cavity pull $\chi'' = \chi''_t + \chi''_e$ into a contribution from the TDQD and EDQD. We note that a negative χ' value leads to photon loss. When $\chi' < \kappa_{\rm tot}$, the photon gain is below threshold and we do not need to consider saturation of the DQDs. The effective cavity linewidth becomes $\tilde{\kappa}_{\rm tot} = \kappa_{\rm tot} - \chi'$, and the resonance frequency becomes $\tilde{f}_c = f_c + \chi''$. The cavity response to a weak cavity input tone can be described by the complex transmission

$$T = \frac{\kappa_{\rm tot}}{\kappa_{\rm tot} - \chi' + 2i(2\pi f_{\rm in} - 2\pi f_c - \chi'')}, \tag{1}$$

where $G = |T|^2$ and the phase shift $\Delta\phi = \arg(T)$. When $\chi' > \kappa_{\rm tot}$, the photon gain triggers maser action and the large photon number may lead to photon saturation of both DQDs.

Our analysis of the threshold behavior is performed separately at the left lead transition of the TDQD and the interdot transition of the TDQD. The left lead charge transition is a transition between a discrete energy level and a Fermi sea of electrons. By contrast, the interdot charge transition involves two discrete levels, and we therefore need to consider the photon saturation of both DQDs.

We first examine the effects of the TDQD on the cavity when the TDQD is at the left lead charge transition and when the EDQD is decoupled from the cavity by placing it in Coulomb blockade. We determine χ' and χ'' based on the cavity response to a weak cavity drive at $f_{\rm in} = f_c$. At the left lead charge transition [indicated by the blue dot in Fig. 4(a)], we measure $G = 0.5$ and $\Delta\phi = 20°$. Equation (1) then estimates $\chi'_t/2\pi = -0.44$ MHz and $\chi''_t/2\pi = -0.4$ MHz. When the EDQD is turned on, there should be no photon saturation effects on the TDQD at the lead transition. In this case, the TDQD and the cavity form an effective cavity with center frequency shifted to $\tilde{f}_c = f_c + \chi''_t/2\pi = f_c - 0.4$ MHz and linewidth broadened to $\tilde{\kappa}_{\rm tot} = \kappa_{\rm tot} - \chi'_t = 2.21$ MHz. The expected frequency pull of 0.4 MHz is in qualitative agreement with a measured frequency shift of 0.2 MHz in Fig. 4(b).

The backaction of the TDQD on the maser emission when the TDQD is at the left lead charge transition can be understood using a previously published theory [24]. The emission efficiency from the EDQD is measured as $\beta = 2.9 \times 10^{-4}$. When the TDQD is tuned to the left lead transition, the threshold current for maser action increases from $I_{\rm th} = 6.1$ nA (see Sec. III) to $\tilde{I}_{\rm th} = \tilde{\kappa}_{\rm tot}/\beta = 7.6$ nA. The measured maser output power $P_{\rm out} = hf_c\kappa_{\rm out}n_c$ depends on n_c, where $\kappa_{\rm out}/2\pi = 0.8$ MHz is the coupling rate to the output port of the cavity. The cavity photon number is theoretically expected to be

$$n_c = \frac{1}{2\xi R/\gamma_e}\left[\frac{I_e}{\tilde{I}_{\rm th}} - 1 + \sqrt{\left(\frac{I_e}{\tilde{I}_{\rm th}} - 1\right)^2 + \frac{4\xi I_e}{\tilde{I}_{\rm th}}}\right], \tag{2}$$

where $\xi = 1 - [(2\alpha I_e)/|e|\tilde{\kappa}_{\rm tot}]$ is a correction parameter associated with the lead emission and $\alpha = 0.3 \times 10^{-4}$. The ratio $R/\gamma_e = \beta - 2\alpha$ compares the photon and phonon spontaneous-emission rates. When the TDQD is tuned to the left lead transition, Eq. (2) estimates $P_{\rm out}$ would be reduced by a factor of 2.7, with the change in $\tilde{\kappa}_{\rm tot}$ based on the above parameters. This estimate is consistent with our measurement, as shown in Fig. 4 (the black line).

We now examine the backaction of the TDQD on the maser emission with the TDQD configured at an interdot charge transition. Here, the TDQD behaves as a two-level system and the large intracavity photon number $n_c = 6000$ saturates the TDQD. We first extract the parameters describing the coupling of the TDQD to the cavity when the EDQD is parked in Coulomb blockade. The TDQD is probed at an interdot charge transition by measuring the response to a weak cavity drive using the method described in Refs. [12,15]. Our estimates are $t_c = 13.5$ μeV, $g_c/2\pi = 25$ MHz, and a decay rate of $\gamma_t/2\pi = 700$ MHz. At zero detuning, the susceptibility of the TDQD is $\chi_t = ig_c^2/[2t_c/\hbar - 2\pi f_c - i(\gamma_t/2)]$. Based on the parameters above, we predict $\chi_t/2\pi = -0.17\text{–}0.53i$ MHz at the interdot charge transition.

In the case of a large cavity photon number n_c we need to consider the saturation of the TDQD. Saturation changes the value of χ_t to $\tilde{\chi}_t = \langle\sigma_z\rangle\chi_t$, where [15,30]

$$\langle\sigma_z\rangle = \frac{-1}{1 + n_c\frac{8g_c^2}{\gamma_t^2 + 4(2t_c/\hbar - 2\pi f_c)^2}}. \tag{3}$$

With the parameters extracted from the input-output theory, we estimate $\langle\sigma_z\rangle = [(-1)/(1 + 0.001n_c)]$. When n_c is small, a full solution for n_c and $\langle\sigma_z\rangle$ can be obtained by solving Eqs. (2) and (3) simultaneously with $\tilde{I}_{\rm th} = I_{\rm th}(1 - \langle\sigma_z\rangle\chi_t/\kappa_{\rm tot})$. However, when n_c is large enough to saturate the TDQD, $\tilde{\chi}_t$ is small, such that $\tilde{I}_{\rm th} \approx I_{\rm th}$. We can then apply a simpler self-consistent analysis, assuming n_c is not changed appreciably from $n_c = 6000$ and thus $\langle\sigma_z\rangle = -1/7$. We estimate $\tilde{\chi}''_t = -38$ kHz, $\tilde{\kappa}_{\rm tot} = \kappa_{\rm tot} - \chi'_t = 1.79$ MHz, and an effective threshold current $\tilde{I}_{\rm th} = 6.16$. Equation (2) self-consistently estimates a change in n_c by 1%. All of these predictions are in reasonable agreement with the measured frequency shift of 37 kHz and the small change in n_c at the interdot charge transition.

E. Charge-state readout through narrow-band measurements of the total cavity output power

The previous section demonstrates that measurements of the emission frequency f_e can be used to reconstruct the TDQD charge stability diagram. However, extracting f_e from measurements of $S(f)$ is too time consuming (3 to 4 s per spectrum) to allow for efficient charge-state readout. The challenge of devising a practical measurement that quickly extracts the state-dependent frequency shift has been solved in the standard readout schemes. For example, in cQED systems, state-dependent shifts in the resonance frequency of the cavity can be measured by driving the cavity with a weak input tone at $f_{\rm in} = f_c$ and detecting the large phase shift $\Delta\phi = \arctan(I, Q)$ of the cavity output field using heterodyne demodulation techniques. As a demonstration of the standard readout approach, Fig. 5(a) plots the phase shift $\Delta\phi$ as a function of V_L^T and V_R^T. Single-dot transitions associated with the left and right dots, as well as the interdot charge transition, are clearly visible in the phase response.

Phase readout is not feasible when EDQD emission is used to populate the cavity with photons since f_e exhibits fluctuations that randomize the phase. Moreover, since f_e is a quantity that depends on the TDQD configuration, the phase shift is not a well-defined quantity. Instead, a quantity analogous to the phase shift can be measured for fast readout. The emission spectrum [Fig. 4(b)] shifts in response to the charge state of the TDQD, allowing us to simply measure the output power $P_{\rm out}$ within a narrow resolution bandwidth (RBW), as schematically illustrated in Fig. 4(b). The frequency range over which the power is integrated $f_e^0 \pm$ RBW/2 should be smaller than the expected state-dependent shift in f_e, yet large enough to tolerate the drift in f_e caused by charge fluctuations in the emitter [24,31]. We operate with RBW > FWHM of the EDQD emission spectrum to tolerate the drift in f_e, and RBW < $|f_e - f_e^0|$ to allow sensitivity to changes in the emission spectrum due to the TDQD charge state. Figure 5(b) shows the output power $P_{\rm out}$ measured around $f_e^0 = 7595.68$ MHz with a 30-kHz RBW. The state-dependent shift in the emission center frequency at a TDQD interdot charge transition leads to a factor of 100 change in $P_{\rm out}$ within the measured bandwidth.

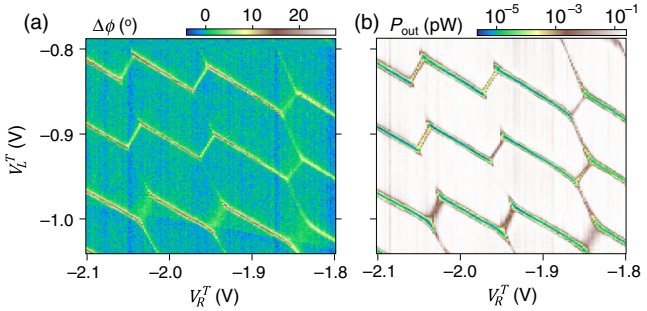

FIG. 5. (a) Cavity phase shift $\Delta\phi$ measured in response to a weak cavity input tone as a function of V_L^T and V_R^T. (b) $P_{\rm out}$ integrated within a 30-kHz RBW as a function of V_L^T and V_R^T. The integrated power in this narrow bandwidth is sensitive to changes in f_e.

V. SUMMARY AND OUTLOOK

In this paper, we show that a voltage-biased DQD can be used as a light source for qubit readout in the cQED architecture. Readout based on measurements of the total output power, emission center frequency, and narrow-band output power are compared. While the total output power is sensitive to single-dot charge transitions, it does not have sufficient sensitivity to resolve interdot charge transitions. Measurements of the emission center frequency reveal both single-dot and interdot charge transitions, but this approach is slow and not well suited for single-shot readout. The narrow-band power measurement approach yields high sensitivity to both single-dot and interdot charge transitions.

In future work, a quantitative understanding of the backaction on the EDQD from the TDQD could be investigated by systematically changing the interdot tunneling rate of the TDQD from below to above the cavity resonance frequency. In some applications, it may be desirable to place the EDQD in a separate cavity. In the masing state, the EDQD generates a large intracavity photon number $n_c \sim 6000$, which may cause saturation effects and broaden the linewidth of the target transition. Separating the emitter from the target qubit would more easily allow the emitted field to be attenuated. It would also be advantageous to reduce the charge noise in our device to levels that have been observed in Si/SiGe DQDs [17], thus improving the linewidth of the maser. Finally, previous work has shown that the maser can be switched on and off rapidly [24]. A switchable maser could be turned off during quantum control sequences and then rapidly activated for high power readout of the qubit state [32]. We hope that this paper will motivate further applications of nanoscale emitters in quantum computing readout architectures.

ACKNOWLEDGMENTS

We thank J. M. Taylor for the helpful discussions and acknowledge support from the Packard Foundation, National Science Foundation Grant No. DMR-1409556, and the Gordon and Betty Moore Foundation's EPiQS Initiative through Grant No. GBMF4535. Devices were fabricated in the Princeton University Quantum Device Nanofabrication Laboratory.

[1] M. Field, C. G. Smith, M. Pepper, D. A. Ritchie, J. E. F. Frost, G. A. C. Jones, and D. G. Hasko, Measurements of Coulomb Blockade with a Noninvasive Voltage Probe, Phys. Rev. Lett. **70**, 1311 (1993).

[2] C. Barthel, M. Kjærgaard, J. Medford, M. Stopa, C. M. Marcus, M. P. Hanson, and A. C. Gossard, Fast sensing of double-dot charge arrangement and spin state with a radio-frequency sensor quantum dot, Phys. Rev. B **81**, 161308 (2010).

[3] J. M. Elzerman, R. Hanson, L. H. Willems van Beveren, B. Witkamp, L. M. K. Vandersypen, and L. P. Kouwenhoven, Single-shot read-out of an individual electron spin in a quantum dot, Nature (London) **430**, 431 (2004).

[4] A. C. Johnson, J. R. Petta, C. M. Marcus, M. P. Hanson, and A. C. Gossard, Singlet-triplet spin blockade and charge sensing in a few-electron double quantum dot, Phys. Rev. B **72**, 165308 (2005).

[5] R. J. Schoelkopf, P. Wahlgren, A. A. Kozhevnikov, P. Delsing, and D. E. Prober, The radio-frequency single-electron transistor (RF-SET): A fast and ultrasensitive electrometer, Science **280**, 1238 (1998).

[6] A. Cottet, C. Mora, and T. Kontos, Mesoscopic admittance of a double quantum dot, Phys. Rev. B **83**, 121311 (2011).

[7] K. D. Petersson, C. G. Smith, D. Anderson, P. Atkinson, G. A. C. Jones, and D. A. Ritchie, Charge and spin state readout of a double quantum dot coupled to a resonator, Nano Lett. **10**, 2789 (2010).

[8] A. Blais, R.-S. Huang, A. Wallraff, S. M. Girvin, and R. J. Schoelkopf, Cavity quantum electrodynamics for superconducting electrical circuits: An architecture for quantum computation, Phys. Rev. A **69**, 062320 (2004).

[9] A. Wallraff, D. I. Schuster, A. Blais, L. Frunzio, R.-S. Huang, J. Majer, S. Kumar, S. M. Girvin, and R. J. Schoelkopf, Strong coupling of a single photon to a superconducting qubit using circuit quantum electrodynamics, Nature (London) **431**, 162 (2004).

[10] M. A. Sillanpaa, J. I. Park, and R. W. Simmonds, Coherent quantum state storage and transfer between two phase qubits via a resonant cavity, Nature (London) **449**, 438 (2007).

[11] M. D. Reed, L. DiCarlo, S. E. Nigg, L. Sun, L. Frunzio, S. M. Girvin, and R. J. Schoelkopf, Realization of three-qubit quantum error correction with superconducting circuits, Nature (London) **482**, 382 (2012).

[12] K. D. Petersson, L. W. McFaul, M. D. Schroer, M. Jung, J. M. Taylor, A. A. Houck, and J. R. Petta, Circuit quantum electrodynamics with a spin qubit, Nature (London) **490**, 380 (2012).

[13] M. R. Delbecq, V. Schmitt, F. D. Parmentier, N. Roch, J. J. Viennot, G. Fève, B. Huard, C. Mora, A. Cottet, and T. Kontos, Coupling a Quantum Dot, Fermionic Leads, and a Microwave Cavity on a Chip, Phys. Rev. Lett. **107**, 256804 (2011).

[14] T. Frey, P. J. Leek, M. Beck, A. Blais, T. Ihn, K. Ensslin, and A. Wallraff, Dipole Coupling of a Double Quantum Dot to a Microwave Resonator, Phys. Rev. Lett. **108**, 046807 (2012).

[15] J. J. Viennot, M. R. Delbecq, M. C. Dartiailh, A. Cottet, and T. Kontos, Out-of-equilibrium charge dynamics in a hybrid circuit quantum electrodynamics architecture, Phys. Rev. B **89**, 165404 (2014).

[16] J. J. Viennot, M. C. Dartiailh, A. Cottet, and T. Kontos, Coherent coupling of a single spin to microwave cavity photons, Science **349**, 408 (2015).

[17] X. Mi, J. V. Cady, D. M. Zajac, P. W. Deelman, and J. R. Petta, Strong coupling of a single electron in silicon to a microwave photon, Science **355**, 156 (2017).

[18] L. E. Bruhat, T. Cubaynes, J. J. Viennot, M. C. Dartiailh, M. M. Desjardins, A. Cottet, and T. Kontos, Strong coupling between an electron in a quantum dot circuit and a photon in a cavity, arXiv:1612.05214.

[19] A. Stockklauser, P. Scarlino, J. V. Koski, S. Gasparinetti, C. K. Andersen, C. Reichl, W. Wegscheider, T. Ihn, K. Ensslin, and A. Wallraff, Strong Coupling Cavity QED with Gate-Defined Double Quantum Dots Enabled by a High Impedance Resonator, Phys. Rev. X **7**, 011030 (2017).

[20] O. Astafiev, K. Inomata, A. O. Niskanen, T. Yamamoto, Y. A. Pashkin, Y. Nakamura, and J. S. Tsai, Single artificial-atom lasing, Nature (London) **449**, 588 (2007).

[21] M. C. Cassidy, A. Bruno, S. Rubbert, M. Irfan, J. Kammhuber, R. N. Schouten, A. R. Akhmerov, and L. P. Kouwenhoven, Demonstration of an ac Josephson junction laser, Science **355**, 939 (2017).

[22] A. Stockklauser, V. F. Maisi, J. Basset, K. Cujia, C. Reichl, W. Wegscheider, T. Ihn, A. Wallraff, and K. Ensslin, Microwave Emission from Hybridized States in a Semiconductor Charge Qubit, Phys. Rev. Lett. **115**, 046802 (2015).

[23] J. Stehlik, Y.-Y. Liu, C. Eichler, T. R. Hartke, X. Mi, M. J. Gullans, J. M. Taylor, and J. R. Petta, Double Quantum Dot Floquet Gain Medium, Phys. Rev. X **6**, 041027 (2016).

[24] Y.-Y. Liu, J. Stehlik, C. Eichler, X. Mi, T. R. Hartke, M. J. Gullans, J. M. Taylor, and J. R. Petta, Threshold Dynamics of a Semiconductor Single Atom Maser, Phys. Rev. Lett. **119**, 097702 (2017).

[25] T. L. van den Berg, C. Bergenfeldt, and P. Samuelsson, Pump-probe scheme for electron-photon dynamics in hybrid conductor-cavity systems, Phys. Rev. B **90**, 085416 (2014).

[26] Y.-Y. Liu, J. Stehlik, C. Eichler, M. J. Gullans, J. M. Taylor, and J. R. Petta, Semiconductor double quantum dot micromaser, Science **347**, 285 (2015).

[27] J. R. Petta, A. C. Johnson, C. M. Marcus, M. P. Hanson, and A. C. Gossard, Manipulation of a Single Charge in a Double Quantum Dot, Phys. Rev. Lett. **93**, 186802 (2004).

[28] M. D. Schroer, M. Jung, K. D. Petersson, and J. R. Petta, Radio Frequency Charge Parity Meter, Phys. Rev. Lett. **109**, 166804 (2012).

[29] C. Eichler, D. Bozyigit, and A. Wallraff, Characterizing quantum microwave radiation and its entanglement with superconducting qubits using linear detectors, Phys. Rev. A **86**, 032106 (2012).

[30] D. F. Walls and G. J. Milburn, *Quantum Optics* (Springer, Berlin, 2008).

[31] Y.-Y. Liu, J. Stehlik, M. J. Gullans, J. M. Taylor, and J. R. Petta, Injection locking of a semiconductor double-quantum-dot micromaser, Phys. Rev. A **92**, 053802 (2015).

[32] M. D. Reed, L. DiCarlo, B. R. Johnson, L. Sun, D. I. Schuster, L. Frunzio, and R. J. Schoelkopf, High-Fidelity Readout in Circuit Quantum Electrodynamics Using the Jaynes-Cummings Nonlinearity, Phys. Rev. Lett. **105**, 173601 (2010).